CHEMISTRY OF MATERIALS

ARTICLE

pubs.acs.org/cm

Nanoporous Silicon Oxycarbonitride Ceramics Derived from Polysilazanes In situ Modified with Nickel Nanoparticles

Mahdi Seifollahi Bazarjani,*[,†] Hans-Joachim Kleebe,[†] Mathis M. Müller,[†] Claudia Fasel,[†] Mehrdad Baghaie Yazdi,[†] Aleksander Gurlo,[†,‡] and Ralf Riedel[†]

[†]Technische Universität Darmstadt, Fachbereich Material-und Geowissenschaften, Petersenstrasse 23, D-64287 Darmstadt, Germany

[‡]School of Engineering and Applied Sciences, Harvard University, 29 Oxford Street, Cambridge, Massachusetts 02138, United States

Supporting Information

ABSTRACT: Ni−polysilazane precursors were synthesized from polysilazane and trans-[bis(2-aminoetanol-N,O)diacetato-nickel(II)]. The Ni−polysilazane precursors are superparamagnetic indicating formation of nanosized nickel particles (~2−3 nm) confirmed by HRTEM as well. The as-obtained Ni−polysilazane precursors were thermolized at 700 °C and transformed to ceramic nanocomposites, manifesting a nanoporous structure, revealing a BET surface area of 215 $m^2 g^{-1}$, a micropore surface area of 205 $m^2 g^{-1}$, and a micropore volume of 0.113 $cm^3 g^{-1}$. Although Si−C−N−(O) ceramics derived from the native polysilazane are nonporous, the pronounced development of porosity in the Ni/Si−C−N−(O) system was attributed to (i) the stabilizing effect of carbosilane bonds, which prohibit the formation of macropores during thermolysis; (ii) the reduced barrier for heterogeneous pore nucleation as a result of in situ created nickel nanoparticles; and (iii) the reduced viscous flow of the pores due to the presence of nickel nanoparticles and turbostratic carbon. The formation of turbostratic carbon is due to the reactions catalyzed by nickel nanoparticles that result in graphene stacking as inferred from the STA−MS studies.

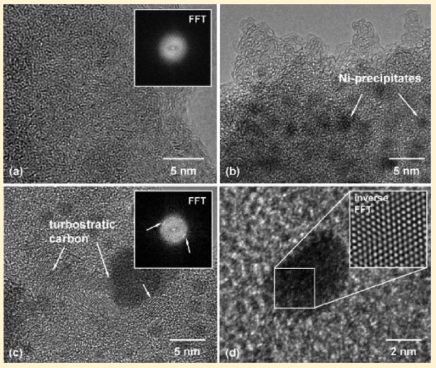

KEYWORDS: micropores, polymer-derived ceramics, polysilazane, nanocomposite, superparamagnetic, graphene stacking, nanosized nickel

INTRODUCTION

Tunable synthesis of ceramics with desired porosity has received considerable attention in the last decades mainly due to their promising functionalities as hydrogen storage materials, molecular sieves and catalysts.[1−13] Silicon-based ceramics in general and micro- and mesoporous silica (SiO_2) in particular have recently attracted large attention. A desired porosity in polymer- and sol−gel-derived SiO_2 is usually achieved through the variation in synthesis and thermolysis conditions.[14−22] An example is polysilazane-derived SiO_2 with micropores of about 0.3 nm in diameter.[23] In another approach, sol−gel-derived SiO_2 embedded with metal nanoparticles preserves a microporous structure and shows reversible hydrogen adsorption and moderate to excellent hydrogen purification capability.[15−21] The drawback of microporous SiO_2 is its degradation under hydrothermal conditions, which limits its applications.[22] Hence, there is a continuous need in the development of novel ceramic materials with desired porosity and stability. Promising candidates are silicon-based polymer-derived ceramics (PDCs), e.g., polysilazane-derived ternary Si−C−N and quarternary Si−C−N−(O) systems, with excellent thermal and chemical stability.[24−27] As the Si−C−N−(O) ceramics, synthesized from native polysilazanes, are usually nonporous, a modification of the polymer composition as well as a proper thermal treatment, i.e., curing and thermolysis of the preceramic polymers under controlled atmosphere, is required for the engineering of PDCs with tailored porosity.[24,28,29] For example, highly microporous Si−C−N ceramics were synthesized via mixing polysilazanes with micrometer-sized Si_3N_4, SiC and AlN fillers and subsequent thermolysis at 700−900 °C in gaseous ammonia.[29] The drawback of this approach is the susceptibility of the resulting silicon imidonitride structure to hydrolysis.[13] Furthermore, micrometer-sized fillers limit the application of the polymer-derived ceramic products in membrane reactors and hydrogen separation modules, which require submicrometer coatings.[22,30]

In the present manuscript, we report a new approach toward desired porosity in Ni/Si−C−N−(O) nanocomposites derived from Ni−polysilazane precursors. The chemical modification of the initial polysilazane structure through desired reactions with an OH-bearing Ni(II) complex changes the mechanism of polymer-to-ceramic transformation resulting in the formation of micro- and mesoporous nanocomposites. In this way, our study provides

Received: August 26, 2010
Revised: August 8, 2011
Published: August 31, 2011

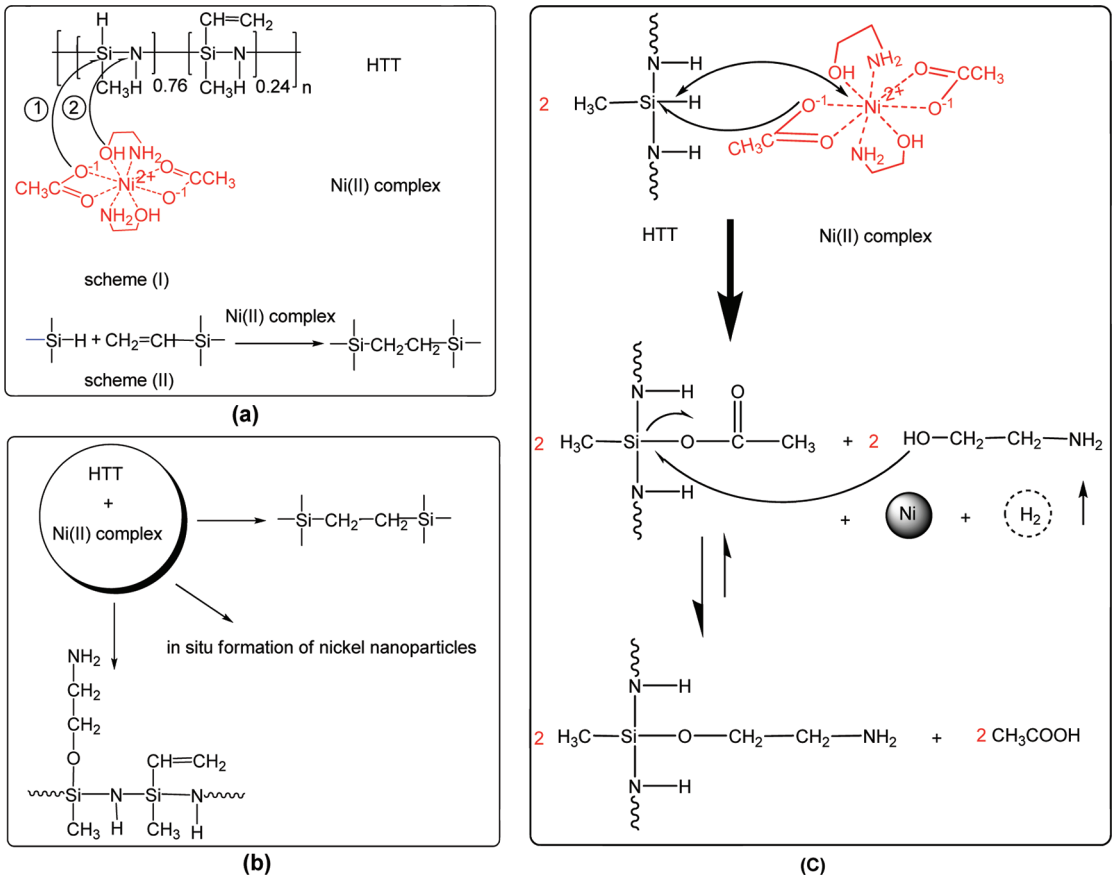

Figure 1. (a) Schematic reaction mechanisms involved in the synthesis of Ni−polysilazane precursors: (I) the reaction between the OH groups of the ethanolamine coordinated by Ni(II) in the Ni(II) complex with the silicon centers of polysilazane HTT, causing the decrease in the number of −Si−NH−Si− linkages in the Ni−polysilazane precursors and the concomitant evolution of gaseous NH_3 during the synthesis of the Ni−polysilazane precursors (see Figure 4 in the Supporting Information for the reaction mechanisms leading to NH_3 evolution); (II) the hydrosilylation reaction between −Si−H and −Si−CH=CH_2 groups in the Ni−polysilazane precursors with the formation of carbosilane bonds, −Si−C−C−Si− (see text for details). (b) Summary of the products after the reaction of polysilazane HTT with the Ni(II) complex; carbosilane bonds, −Si−O−CH_2−CH_2−NH_2 bonds, and in situ nickel nanoparticles formation. (c) Proposed reaction mechanism for the in situ formation of nickel nanoparticles involving electron transfer from partially negative charged hydrogen in Si−H group to Ni^{2+} in the Ni(II) complex.

Table 1. Amount of the Ni(II) Complex Used for the Synthesis of the Ni−Polysilazane Precursors (S1, S2, and S3) and the Elemental Composition of Si−C−N−(O) and Ni/Si−C−N−(O) Nanocomposites Derived Therefore

sample	polysilazane HTT	S1	S2	S3
Ni(II) complex (wt %)		6.3	27.0	40.0
Ni (wt %)	0	0.96	4.43	8.87
Si (wt %)	45.05	41.95	33.00	33.15
C (wt %)	18.83	16.75	19.59	20.10
N (wt %)	16.21	11.77	6.55	3.32
O (wt %)	13.34	20.18	31.19	28.43
H (wt %)	3.5	2.7	2.6	2.16
empirical formula	$Si_1C_{0.97}N_{0.71}O_{0.62}H_{2.17}$	0.011 $Ni/Si_1C_{0.93}N_{0.56}O_{0.84}H_{1.80}$	0.064 $Ni/Si_1C_{1.385}N_{0.40}O_{1.65}H_{2.21}$	0.13 $Ni/Si_1C_{1.41}N_{0.20}O_{1.5}H_{1.83}$

a fundamental approach on how to transform polymer-derived ceramics into hybrid nanoporous materials underlying mechanisms involved in the development of the porosity in Ni/Si−C−N−(O) nanocomposites.

EXPERIMENTAL METHODS

Materials. Ni/Si−C−N−(O) composites were synthesized by the reaction of a commercially available polysilazane (HTT 1800, KiON Specialty Polymers, polysilazane HTT hereafter, see Figure 1a) reacted with trans-[bis(2-aminoetanol-N,O)diacetato-nickel(II)] (synthesized in our laboratory, Ni(II) complex hereafter) in anhydrous tetrahydrofuran (≥99.98, Sigma Aldrich). All reactions were carried out under inert atmosphere (99.999% argon).

Polysilazane HTT Specifications. The molecular gel permeation chromatography (GPC) of the polysilazane HTT dissolved in tetrahydrofuran indicated a multimodal molecular mass distribution with a strong signal below 250 g mol^{-1} and M_n = 208, M_w = 264, and M_z = 620 g mol^{-1}.

dx.doi.org/10.1021/cm200589n |*Chem. Mater.* 2011, 23, 4112–4123

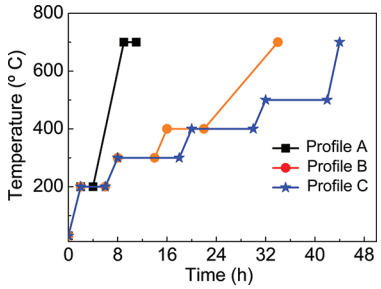

Figure 2. Temperature profiles A, B, and C, used for the thermolysis of the Ni−polysilazane precursors S1, S2, and S3.

Elemental analysis gave a composition (wt %) of 43.5 Si, 22 N, 26 C and 8.4 H that corresponds to the empirical formula $Si_{0.11}N_{0.11}C_{0.16}H_{0.61}$ with trialkylsilyl/hydrosilyl as the end groups.[31,32]

Synthesis of Ni(II) complex. The Ni(II) complex was synthesized in our laboratory (Figure 1a) using nickel(II) acetate tetrahydrate (≥99.0%, Sigma Aldrich), ethanolamine (≥99.0%, Sigma Aldrich) and absolute ethanol (≥98, Sigma Aldrich). Nickel(II) acetate tetrahydrate was dissolved in absolute ethanol and mixed with ethanolamine in a molar ratio of 1:3. The resulting bluish clear solution was stirred in air for 24 h and used for the crystallization of single crystals of the blue Ni(II) complex, which was separated from the solution, washed, and dried in air at 40 °C. The single-crystal XRD pattern (Xcalibur diffractometer with Mo K_α radiation) confirmed the formation of trans-[bis(2-aminoetanol-N,O)diacetato-nickel(II)].

Synthesis of Ni−Polysilazane Precursors. Three precursors with different initial content of the Ni(II) complex, i.e., 6.3 (sample S1, see Table 1), 27.0 (sample S2,) and 40.0 wt % (sample S3), were synthesized according to the following procedure. Prior to synthesis, the Ni(II) complex was dried under vacuum at 18 Pa for at least 5 h at 40 °C and directly transferred to the glovebox. After the addition of an appropriate amount of polysilazane HTT to the desired amount of the Ni(II) complex the reaction vessel was immediately removed from the glovebox and submerged in an ice bath. Then anhydrous tetrahydrofuran (THF) was added to the reaction vessel under rapid flow of Ar, kept in the ice bath, and the as-resulted solution was stirred for 5 to 7 h. Afterward the temperature was increased to 14−17 °C by placing the reaction vessel into an 2-propanol bath and the synthesis was continued under slow Ar flow using standard Schlenk technique until the end of the ammonia liberation. The color of the reaction mixture changed from blue to green and at the end of the reaction the color became dark brown (see Figure 6 in the Supporting Information). Finally, the THF was removed under vacuum at 40 °C for at least 5 h and the Ni−polysilazane precursors were collected in the glovebox.

Synthesis of Ni/Si−C−N−(O) Nanocomposites. Thermolysis of the as-synthesized Ni−polysilazane precursors was performed in a tube furnace under flowing Ar (approximately 75 mL/min) applying three different temperature (thermolysis) profiles. The profiles are denoted as Profile A, Profile B, and Profile C (Figure 2).

Profile A: the precursors were heated to 200 °C with a rate of 100 °C h^{-1}, hold for 2 h at 200 °C, from 200 °C with a rate of 100 °C h^{-1} to 700 °C, hold for 2 h at 700 °C, and finally cooled to room temperature with a rate of 50 °C h^{-1}.

Profile B: the precursors were heated from room temperature with a rate of 100 °C h^{-1} to 200 °C, hold for 4 h at 200 °C, further heated to 300 °C with a rate of 50 °C h^{-1}, hold for 6 h at 300 °C, further heated to 400 °C with a rate of 50 °C h^{-1}, hold for 6 h at 400 °C, further heated to 700 °C with a rate of 25 °C h^{-1}, and finally cooled to room temperature with a rate of 50 °C h^{-1}.

Profile C: the precursors were heated from room temperature with a rate of 100 °C h^{-1} to 200 °C, hold for 4 h at 200 °C, further heated to 300 °C with a rate of 50 °C h^{-1}, hold for 10 h at 300 °C, further heated to 400 °C with a rate of 50 °C h^{-1}, hold for 10 h at 400 °C, further heated to 500 °C with a rate of 50 °C h^{-1}, hold for 10 h at 500 °C, further heated to 700 °C with a rate of 100 °C h^{-1}, and finally cooled to room temperature with a rate of 50 °C h^{-1}.

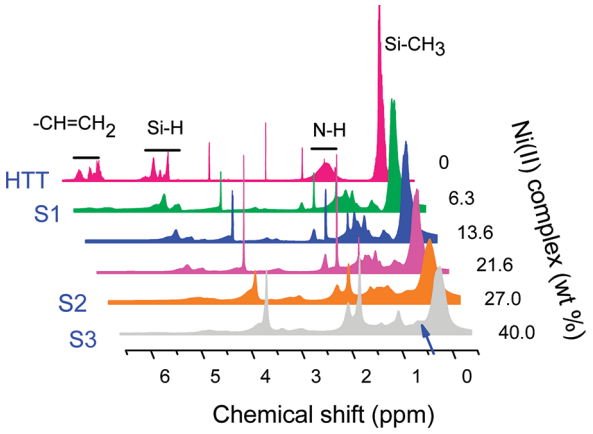

Figure 3. ^1H NMR spectra of the polysilazane HTT and the Ni−polysilazane precursors S1, S2, and S3. An arrow points out at the chemical shift, which confirms the formation of $-OSiCH_3$ bonds.

As the thermolysis Profile C resulted in the formation of Ni/Si−C−N−(O) nanocomposites with the highest surface area and micropore volume (see text for details), only Ni/Si−C−N−(O) nanocomposites obtained from the thermolysis Profile C were subjected to a detailed structural characterization as described in the section Structure of Ni/Si−C−N−(O) Nanocomposites.

Characterization. ^1H, ^{13}C, ^{29}Si, and 2D ^1H, ^{13}C HSQC (heteronuclear single quantum coherence) NMR spectra were recorded on a Bruker DRX 500 MHz spectrometer using specimens dissolved in THF−d^8. 2D ^1H, ^{13}C HSQC spectra were collected with 2048 points in f2 and 256 points in f1 over a bandwidth of 10 ppm in ^1H and 180 ppm in ^{13}C with four scans per f1 value and a recycle time of 2 s (giving a total acquisition time of ca. 1 h).

Raman spectra were recorded on a confocal Horiba HR800 Raman microscope by using an excitation laser with a wavelength of 514.5 nm. FT-IR spectra were recorded on a Nicolet Nexus 470 FTIR spectrometer with a nitrogen-purged optical bench (Nicolet, Madison, WI) equipped with a DTGS detector. X-ray diffractograms were obtained by a STOE X-ray diffractometer with Ge (111) monochromator and Mo K_α radiation.

Simultaneous thermal analysis coupled with mass spectrometry (STA−MS) was performed using a Simultaneous Thermoanalyzer Netzsch STA 449 C Jupiter and a Quadrupole mass spectrometer QMS 403 C Aëolos with a heating rate of 5 °C/min under argon atmosphere and a gas flow of 250 mL/min. Chemical analysis of carbon, nitrogen and oxygen was carried out using GMBH C-200 (carbon analyzer, Leco Instrumente) and TC-436 (nitrogen and oxygen analyzer, Leco Instrumente). The nickel, silicon, and hydrogen contents were determined at the Mikroanalytisches Labor Pascher (Remagen, Bendorf-Germany) applying the coupled plasma atomic emission spectroscopy (Thermo Instruments, iCAP 6500) and elementanalyzer (Pascher). The results of the elemental analysis are given in Table 1.

Pore volume and surface area analysis of the selected ceramic powders were carried out according to Brunauer−Emmett−Teller (BET) method by N_2 sorption isothermal analysis at −196 °C (77 K, Model Autosorb-1, Quantachrome Instruments, USA) after powdered samples were outgassed at 150 °C for 24 h. Microporosity analysis of ceramic powders was evaluated by adsorbed layer thickness method (t-method).

High resolution transmission electron microscopy (HRTEM) was performed at a FEI CM20STEM instrument operated at 200 kV (FEI, Eindhoven, The Netherlands). Sample preparation involved dispersing

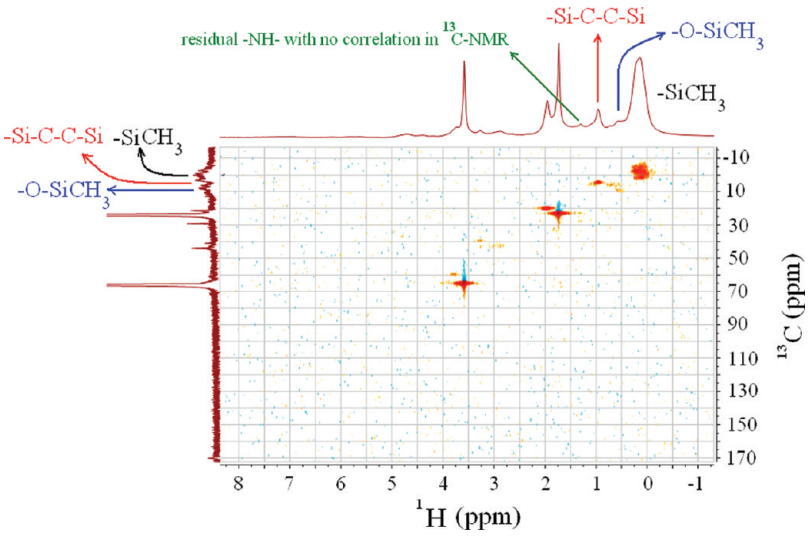

Figure 4. 2D ^{1}H, ^{13}C HSQC spectra of the Ni−polysilazane precursor S3, revealing the formation of −Si−C−C−Si− and −O−SiCH$_3$ bonds.

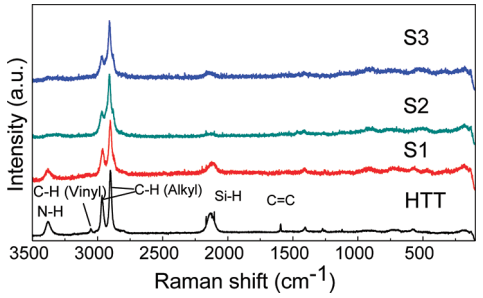

Figure 5. Micro-Raman spectra of the polysilazane HTT and the Ni−polysilazane precursors S1, S2, and S3 with the Ni(II) complex content of 6.3, 27, and 40 wt % used in the synthesis, respectively, manifesting the decrease in Si−H, −CH=CH$_2$ and −NH− bonds in the Ni−polysilazane precursors.

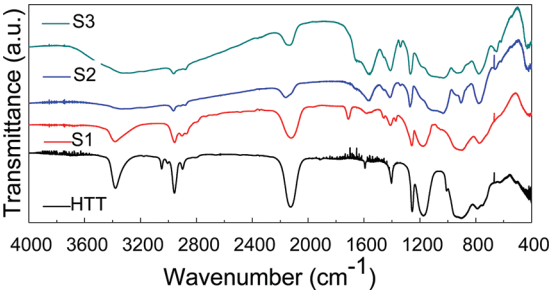

Figure 6. FTIR spectra of the polysilazane HTT, and the Ni−polysilazane precursors S1, S2 and S3 with the Ni(II) complex content of 6.3, 27, and 40 wt % used in the synthesis, respectively.

the powder in ethanol and deposing the dispersion on a carbon coated Cu-grid (Plano, Germany), followed by light carbon coating to minimize charging under the incident electron beam.

Magnetic properties were studied using a magnetic property measurement system (MPMS, Quantum Design) utilizing a superconducting quantum interference device (SQUID). Magnetic behavior was studied for a temperature range of −260 to 25 °C with a constant applied field, furthermore the magnetization as a function of applied field (from −15 000 to 15 000 Oe) was recorded at 25 °C.

The molecular weight distribution of the polysilazane HTT was determined by gel permeation chromatography (GPC) on a Waters system. The eluting solvent was HPLC grade THF at a flow rate of 1.2 mL/min. The retention times were calibrated against known monodisperse polystyrene standards, 18700, 5120, 2200, 1200, and 870, with M_w/M_n values <1.09.

RESULTS AND DISCUSSION

Structure of Ni−Polysilazane Precursors and the Reaction Mechanism Involved in Their Synthesis. The comprehensive ^{1}H (Figure 3), ^{13}C (Figure 1 in the Supporting Information), ^{29}Si (Figure 2 in the Supporting Information) and 2D ^{1}H, ^{13}C HSQC (Figure 4) NMR, Raman (Figure 5), FTIR (Figure 6), XRD (Figure 7), SQUID (Figure 8), and HRTEM (Figure 9) characterization of as-synthesized Ni−polysilazane compounds implies that the polysilazane HTT structure is massively influenced through reaction with the Ni(II) complex. Basically, three main effects are implied: (A) the reaction between the OH groups of the ethanolamine coordinated by Ni(II) in Ni(II) complex with the silicon centers of the polysilazane HTT resulting in the decrease of number of −Si−NH−Si− linkages in the Ni−polysilazane precursors and in the evolution of gaseous H_2 and/or NH_3 (Figure 1a, scheme I, and Figure 4 in the Supporting Information) (B) the hydrosilylation reaction between −Si−H and vinyl (−Si−CH=CH$_2$) groups in the Ni−polysilazane precursors resulting in the formation of carbosilane bonds, −Si−C−C−Si− (Figure 1a, scheme II), and (C) reduction of Ni^{2+} and in situ formation of nickel nanoparticles distributed in the polymeric matrix (Figure 1c). The summary of the main reaction products is mentioned in Figure 1b.

As analyzed from the ^{1}H NMR spectra (Figure 3), the intensity of the −Si−H and −Si−CH=CH$_2$ groups with the chemical shift at ∼4.5 and ∼6 ppm, respectively, is considerably reduced in the Ni−polysilazane precursors if compared to those in the polysilazane HTT. Furthermore, the 2D ^{1}H, ^{13}C NMR spectra show that the decrease in intensity (in S1 and S2) and the disappearance (in S3) of the −Si−H and −Si−CH=CH$_2$ groups are accompanied by the formation of −Si−C−C−Si− units

dx.doi.org/10.1021/cm200589n |Chem. Mater. 2011, 23, 4112–4123

(Figure 4). The observed chemical shifts at 1.12−0.78, 9.91−4.01, and −21.90 ppm for ^{1}H NMR, ^{13}C NMR, and ^{29}Si NMR, respectively, are in a good agreement with those reported previously for carbosilane dendrimers.[33] It is important to note that in pure polysilazanes, the hydrosilylation occurs at T > 120 °C,[32,34] whereas in the Ni−polysilazane precursors, the carbosilane bonds already form at room temperature. This finding clearly indicates the catalytic activation of the hydrosilylation reaction by the Ni(II) complex similar to previous reports on other nickel containing catalysts.[35−37] A competitive vinyl addition reaction via vinyl groups[38−40] is less probable because in pure polysilazanes it requires much higher temperature of about 400 °C compared to 120 °C needed for hydrosilylation.[34]

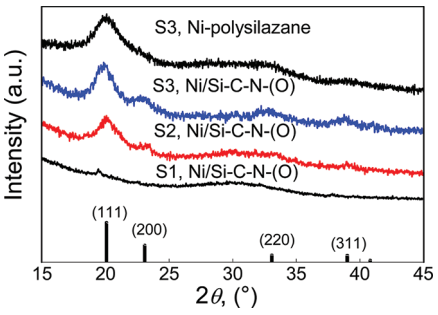

Figure 7. XRD patterns of the Ni−polysilazane precursor S3 before thermolysis and Ni/Si−C−N−(O) nanocomposites after the thermolysis of the Ni−polysilazane precursors S1, S2, and S3 with the Ni(II) complex content of 6.3, 27, and 40 wt % used in the synthesis, respectively. At the bottom the diffraction pattern of nickel (ICDD PDF 65−2865, space group $Fm\bar{3}m$ (No. 225), a = 3.5240 Å) is shown.

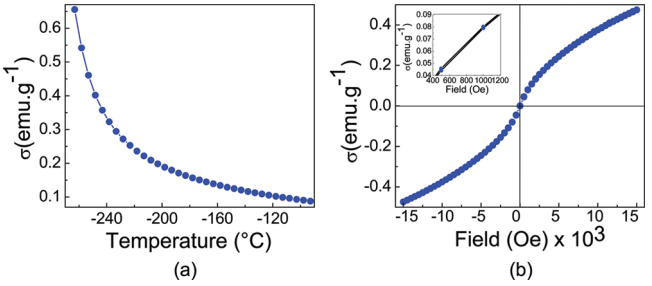

Figure 8. (a) Magnetization of the Ni−polysilazane precursor S3 as a function of temperature. (b) Field dependence of the magnetization recorded at 25 °C indicating typical superparamagnetic character confirming the formation of nickel nanoparticles in the Ni−polysilazane precursor S3. Inset, close-up of field dependence of the magnetization in 400−1200 Oe range emphasizing lack of area under the curve.

The reaction between the OH groups of the ethanolamine coordinated by Ni(II) in Ni(II) complex with the silicon centers of the polysilazane HTT (Figure 1a, scheme I, and Figure 4 in the Supporting Information) is confirmed by (a) the 2D ^{1}H, ^{13}C NMR spectra (Figure 4) and by (b) an additional experiment involving polysilazane HTT and ethanolamine (Figure 3 in the Supporting Information). An appearance of the −OSiCH$_3$ chemical shift at 0.70−0.40 ppm is found in the ^{1}H NMR spectra of the Ni−polysilazane precursors, i.e., at slightly higher values than that of the −SiCH$_3$ in the polysilazane HTT (0.417 to −0.05 ppm). The shift downfield of about 0.5 −0.4 ppm, indicated with an arrow in Figure 3, is due to the electron withdrawing by the substituted OH groups in ethanolamine (−O−SiCH$_3$). The N−H chemical shift in the polysilazane HTT (bs, 1.66−0.824 ppm in the ^{1}H NMR spectra, Figure 3) is gradually replaced by a chemical shift at 1.12−0.78 ppm and residual N−H chemical shift at 1.4−1.2 ppm in the Ni−polysilazane precursors.

The Raman (Figure 5) and FTIR (Figure 6) spectra confirm the proposed reaction mechanisms (Figure 1 here and Figure 4 in the Supporting Information). Thus, the decrease in number of −Si−NH−Si− linkages in Ni−polysilazane precursors is analyzed also via the decrement in the intensity of the −Si−NH−Si− bands (Figure 5). The polysilazane HTT shows Raman bands at 3383 cm^{-1} (−NH−), 3052 cm^{-1} (−CH=CH$_2$), 2965 and 2902 cm^{-1} (−CH$_3$), 2140 cm^{-1} (Si−H), and 1593 cm^{-1} (−CH=CH$_2$). In the Ni−polysilazane precursors, the Raman band intensities related to −NH−, Si−H and vinyl groups are drastically reduced, which is in agreement with the ^{1}H NMR results (Figure 3). In the polysilazane HTT the following IR bands are found: the bands related to vinylsilyl groups (CH$_2$=CHSi−) are found as C−H vibrations at 3046 and 3006 cm^{-1}, and C=C stretching at 1592 cm^{-1} (Figure 6). A strong Si−H absorption band appears at 2129 cm^{-1}. The bands ascribed to −Si−NH−Si− groups include N−H stretching at 3379 cm^{-1} and Si−N vibrations at 1173 cm^{-1}. Si−CH$_3$ groups were detected by their characteristic band at 1255 cm^{-1}, together with methyl C−H vibrations at 2957 and 2896 cm^{-1}.

In the Ni−polysilazane compounds, the intensities of the C−H vibration at 3046 cm^{-1} and 3006 cm^{-1} related to the vinyl group, as that of Si−H and −NH− (in −Si−NH−Si−) groups

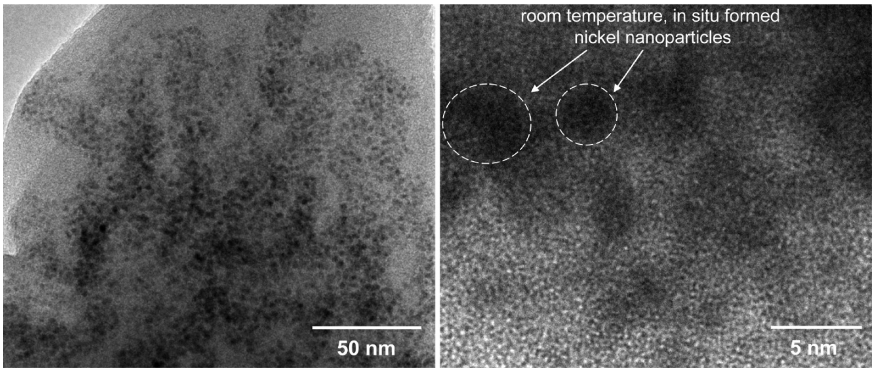

Figure 9. TEM (left) and HRTEM (right) images of the Ni−polysilazane precursor S3 showing the in situ formed nickel nanoparticles in the polysilazane matrix modified via reaction with the Ni(II) complex.

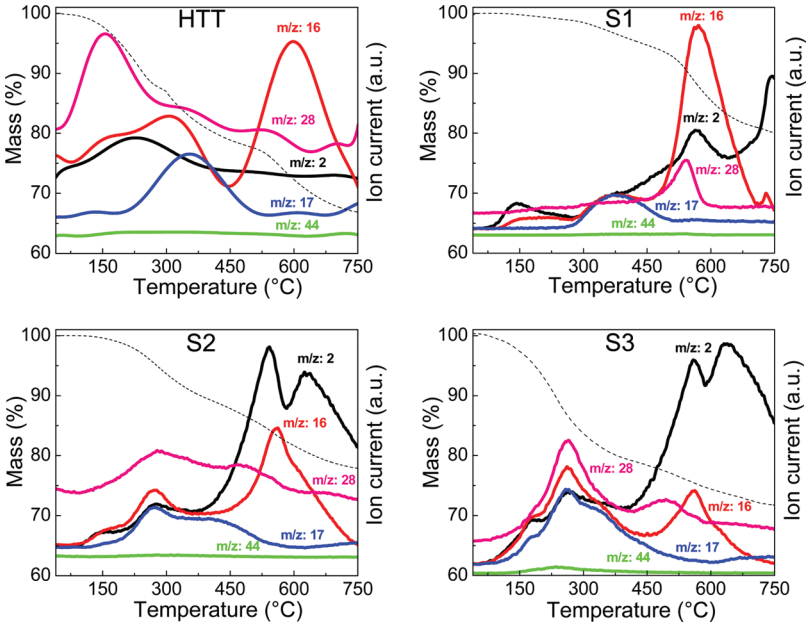

Figure 10. Results of simultaneous thermal gravimetry (dashed lines) − mass spectrometry analysis of the polysilazane HTT and the Ni−polysilazane precursors S1, S2 and S3. Part 1: evolution of species with m/z = 2 (black), 16 (red), 17 (blue), 28 (pink), and 44 (green).

are reduced confirming our ^{1}H NMR and Raman results. At the same time the intensity of new IR bands related to C═O vibration, 1590−1570 cm^{-1}, of the acetate anion and N−H bending from ethanolamine, 1710 cm^{-1}, grow with increasing content of Ni(II) complex.

Simultaneously with the structural modification of the polysilazane HTT, the Ni^{2+} in the Ni(II) complex is being reduced at room temperature forming nanosized nickel particles dispersed in the polymeric matrix as confirmed by XRD (Figure 7, top) as well as by SQUID measurement (Figure 8). High-resolution transmission electron microscopy (HRTEM) studies unambiguously exhibit the distribution of the nickel nanoparticles in the modified polysilazane matrix (Figure 9). The XRD pattern of the Ni−polysilazane precursor S3 manifests vague reflections of metallic nickel (ICDD-PDF-65−2865, space group *Fm*3*m* (No. 225), a = 3.5240 Å). The SQUID characterization of the same specimen indicates a superparamagnetic behavior (details are given in the following paragraph), which is due to the in situ formed nickel nanoparticles homogeneously distributed in the nonmagnetic amorphous polysilazane matrix. The nickel nanoparticles are most probably formed either (i) due to the in situ reduction of Ni^{2+} in the Ni(II) complex by hydrogen released from the nucleophilic substitution of −OH groups of the ethanolamine in the Ni(II) complex at the Si−H sites of the polysilazane HTT (see Figure 4 and 5 in the Supporting Information)[41] or (ii) due to the reaction between the Ni(II) complex and the Si−H bonds of the polysilazane HTT as suggested in Figure 1c.[42,43]

The SQUID measurement shown in Figure 8a reveals a typical characteristic for paramagnetic samples. Ferromagnetic magnetization curve can not be detected in the full temperature range. This finding is a clear indication that the nickel is present only below a critical size, which leads to the so-called superparamagnetic state, common to ferromagnetic materials, when present as nanoparticles. Field dependence of the magnetization further confirms the latter results (Figure 8b) showing no hysteresis loop, a close up can be seen in the inset, which is a definite proof of superparamagnetism indicating the formation of very small nickel nanoparticles. Nickel nanoparticles with sizes above ∼10 nm would show a strong ferromagnetic signal,[44] which is well detectable in the highly sensitive SQUID measurement setup, since the SQUID signal is an average over the entire sample and a nonlocal method. Thus, it can be concluded that all the nickel nanoparticles are below the critical size. HRTEM images further confirm the latter conclusion (Figure 9).

Simultaneous Thermal Analysis-Mass Spectrometry (STA-MS) Characterization during the Transformation of Ni−Polysilazane Precursors into Ni/Si−C−N−(O) Nanocomposites. The thermolysis of the polysilazane HTT (Figure 10) is accompanied by the evolution of gaseous H_2 (m/z = 2), CH_4 (m/z = 16) and NH_3 (m/z = 17) as well as by the distillation of oligomer fragments (m/z = 41−44). The H_2 evolution (maximum at ∼250 °C) is due to the dehydrocoupling reactions of Si−H/Si−H and Si−H/N−H groups−with simultaneous distillation of oligomer fragments that condense in the capillary before reaching the MS detector[32]−which are responsible for the weight loss of ∼12.4% at T < 300 °C. The NH_3 evolution (maximum at ∼350 °C) corresponds to transamination reactions causing a weight loss of ∼9.6% at 300−530 °C.[3,34,45] The CH_4 evolution (maximum at ∼600 °C) originates from either the decomposition of Si-CH_3 groups or the cleavage of C−C bonds providing a weight loss of ∼12% at 530−750 °C.[34] The distillation of oligomer fragments (m/z = 41−44, maximum at ∼150−250 °C) is confirmed by the detection of Si−H bonds at 2140 cm^{-1} analyzed via in situ FTIR measurements and was reported for other polysilazanes as well.[45]

The thermolysis of the Ni−polysilazane precursors S1, S2, and S3 (Figures 10 and 11) differs significantly from that of the polysilazane HTT both concerning the nature as well as kinetics of the evolved gaseous species (for more details, see the Supporting Information) and is in agreement with the suggested structural modifications of the Ni−polysilazane precursors. The first remarkable difference is the substantial increase in H_2 evolution

dx.doi.org/10.1021/cm200589n |*Chem. Mater.* 2011, 23, 4112–4123

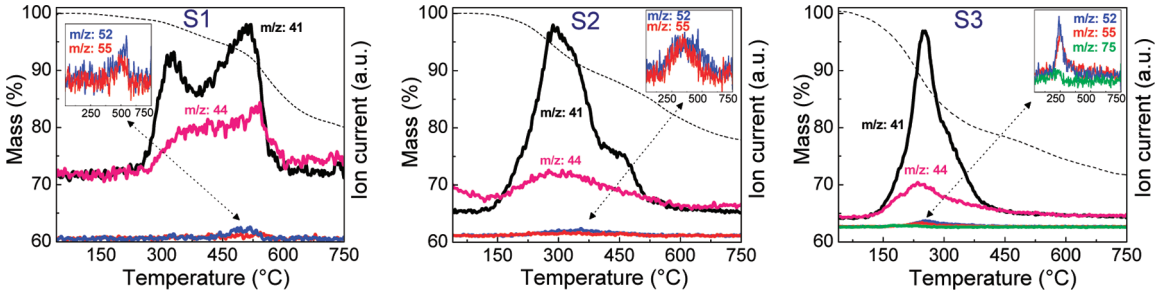

Figure 11. Results of simultaneous thermal gravimetry (dashed lines)—mass spectrometry analysis of the Ni—polysilazane precursors S1, S2, and S3. Part 2: evolution of species with m/z = 41 (black), 44 (pink), 52 (blue), 55 (red), and 75 (green).

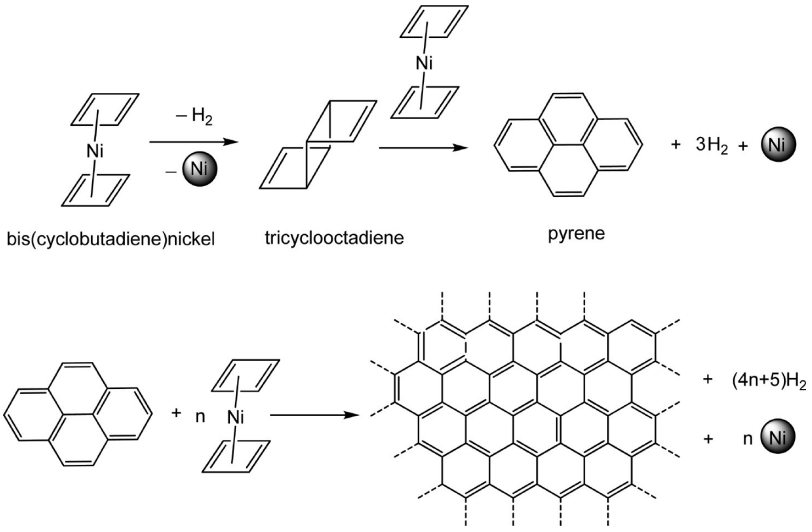

Figure 12. Scheme of the catalytic formation of graphene from transient nickel cyclobutadiene complex; the subsequent stacking of the graphene layers results in the formation of turbostratic carbon.

at T > 400 °C, which increases with higher nickel content. This finding is explained by the activation of dehydrogenation reactions by nickel nanoparticles.[46] The second difference is the shift in the NH_3 evolution to lower temperatures (~260 °C) if compared to that of the native polysilazane HTT (~350 °C); the reduced temperature of NH_3 evolution is due to the decomposition of $-Si-O-(CH_2)_2-NH_2$ groups formed in the Ni—polysilazane precursors (see Figure 1 here and Figure 4 in the Supporting Information). The third and the most interesting difference is the evolution of species with m/z = 50—58 at 250—550 °C; the highest intensity was observed for m/z = 52 with a maximum at 543, 355, and 253 °C for S1, S2, and S3 precursors, respectively (Figure 11).

As these species were not found during the thermolysis of pure polysilazane HTT and the m/z values between 50 and 58 are related to the evolution of hydrocarbons C_4H_x (x = 2—10), it is logically to conclude about the formation of hydrocarbons catalyzed by the in situ formed nickel nanoparticles which has to be considered here.[29,47,48] Indeed, the species with m/z = 52 is ascribed to $C_4H_4^+$ emanating from ionization of cyclobutadiene,[49—53] which is an unstable compound,[54,55] and its detection in the gas-phase by mass-spectrometry from ionized acetylene clusters, $(C_2H_2)^+_n$ (including $C_4H_4^+$) was reported.[56] This finding explains the formation of turbostratic carbon in Ni/Si—C—N—(O) nanocomposites (see next section). Nickel nanoparticles formed in the Ni—polysilazane precursors S1, S2, and S3 could facilitate the formation of the nickel—cyclobutadiene complexes such as bis(cyclobutadiene)nickel.[57—60] Additionally, nickel catalyzes the formation of species such as pyrene.[61] Transient nickel—cyclobutadiene complexes could undergo further dimerization[62] and polymerization to form graphene layers that, after stacking, finally results in the formation of turbostratic carbon (Figure 12).

Structure of Ni/Si—C—N—(O) Nanocomposites. The thermolysis of Ni—polysilazane precursors in argon is completed at 800 °C as confirmed by the thermal analysis (see previous section and Figure 7 in the Supporting Information). The Ni—polysilazane precursors manifest higher ceramic yields at ~800 °C as compared to that of the polysilazane HTT because of the formation of carbosilane bonds, which are not affected by the main chain depolymerization through transamination and exchange of Si—N bonds during the thermolysis of polysilazanes.[3,34]

The XRD patterns of the thermolized Ni—polysilazanes, i.e., Ni/Si—C—N—(O) nanocomposites, reveal the presence of an amorphous Si—C—N—(O) matrix containing embedded nanocrystalline nickel particles (ICDD-PDF-65-2865, space group $Fm3m$ (No. 225), a = 3.5240 Å) (Figure 7). HRTEM analyses of the two samples (i) the polysilazane HTT and (ii) the Ni—polysilazane S3 after thermolysis confirm that the reference material (i.e., ceramic derived from the polysilazane HTT) is

dx.doi.org/10.1021/cm200589n |*Chem. Mater.* 2011, 23, 4112–4123

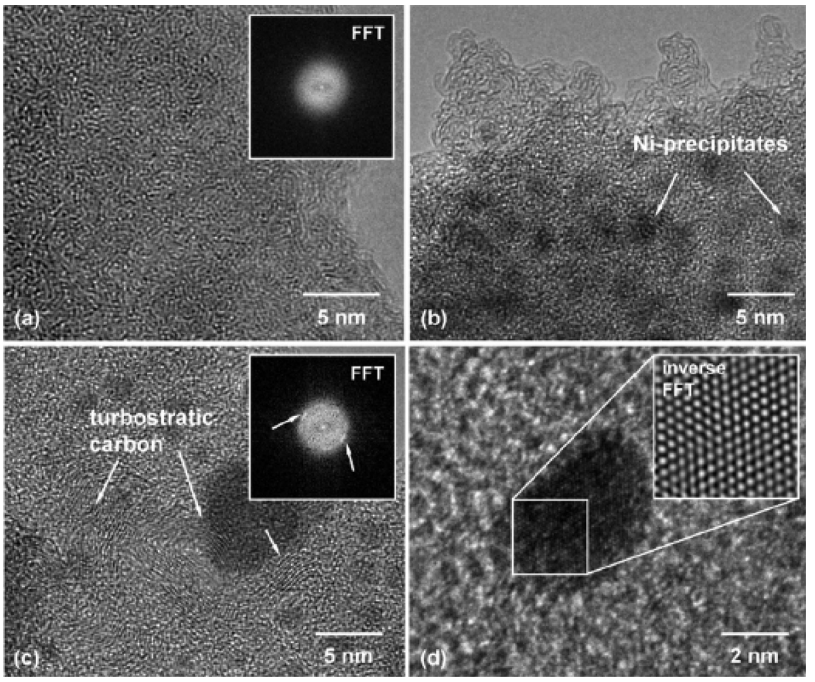

Figure 13. HRTEM images of the thermolysis product of the (a) polysilazane HTT (reference sample) and that of the (b–d) Ni–polysilazane precursor S3 with the Ni(II) complex content of 40 wt % upon thermolysis at 700 °C. The thermolysis product of the polysilazane HTT is fully amorphous, as indicated by the inset (diffraction patterns obtained by Fourier filtered transform (FFT)). In contrast to a, the Ni/Si–C–N–(O) nanocomposite revealed a dark, spherical contrast resulting from the precipitation of crystalline nickel nanoparticles, 2–3 nm in diameter. Note that in the Ni/Si–C–N–(O) nanocomposite the turbostratic carbon was observed throughout the entire sample, suggesting a strong catalytic reaction of the nickel nanoparticles. No lattice fringes or lattice points are seen in the nickel nanoparticles in b and c; however, when using a rather high defocus setting of the objective lens (first pass band), the crystallinity of even very small nanoparticles could be verified in d.

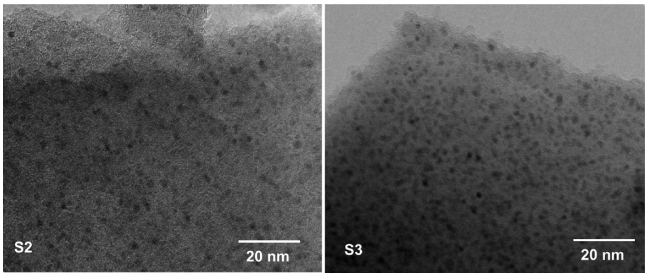

Figure 14. Low-magnification TEM images of the Ni/Si–C–N–(O) nanocomposites obtained from the Ni–polysilazane precursors S2 and S3 showing homogeneous distribution of the nickel nanoparticles with 2–3 nm in diameter.

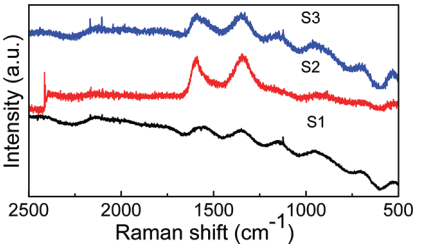

Figure 15. Raman spectra of the thermolysis products (i.e., Ni/Si–C–N–(O) nanocomposites) of the Ni–polysilazane precursors S1, S2, and S3 with the Ni(II) complex content of 6.3, 27, and 40 wt % used in the synthesis, respectively.

completely amorphous with no residual (nano)porosity visible within the bulk (Figure 13a). The thermolysis product of the Ni–polysilazane precursor S3 is predominantly amorphous; however, a dark, spherical contrast is clearly visible, which verifies the precipitation of small, 2–3 nm in diameter sized nickel nanoparticles (Figure 13b). It should be noted that in Figure 13b, no lattice fringes or lattice points are seen; however, when using a rather high defocus setting of the objective lens (1st pass band), the crystallinity of even the very small nickel nanoparticles could be verified (Figure 13d). Low-magnification TEM images indicates similar size and homogeneous distribution of nickel nanoparticles in the Ni/Si–C–N–(O) nanocomposites obtained from the Ni–polysilazane precursors S2 and S3 (Figure 14). No changes in the size as well as in the distribution of the nickel nanopartilces were observed.

The most intriguing feature of the Ni/Si–C–N–(O) nanocomposites is the presence of free carbon, as shown in Figure 13c. Typically, upon thermolysis at temperatures ranging between 800 and 900 °C, the excess of free carbon phase is not yet found in polysilazane based ceramics and higher thermolysis temperatures are required to initiate the formation and the precipitation of turbostratic carbon.[63–66] In the presence of nickel nanoparticles, the formation of free carbon was confirmed at a temperature as low as 700 °C. The mechanism of the precipitation of turbostratic carbon is described in the previous section (Figure 12). Note that the carbon phase shown in Figure 13c, indicated by arrows, was found throughout the entire volume of the sample.

The precipitation of turbostratic carbon is also confirmed by the appearance of the D and G bands at approximately

dx.doi.org/10.1021/cm200589n |*Chem. Mater.* 2011, 23, 4112–4123

1350 cm^{-1} and 1582 cm^{-1}, respectively, in the Raman spectra (Figure 15) which are due to in-plane bond stretching of sp^2 carbon.[63] The C/H and O/N ratios in the as synthesized Ni/Si−C−N−(O) nanocomposites increases simbatly with the nickel content (Figure 17a). The increase in the C/H ratio is explained by the dehydrogenation active nickel nanoparticles which increase the ratio of sp^2 to sp^3 carbon as confirmed by the Raman spectra (Figure 15) and by the observation of turbostratic carbon in HRTEM (Figure 13). The increase in the O/N ratio is due to the nucleophilic substitution of −OH from the ethanolamine in the Ni(II) complex at the Si centers of polysilazane HTT, replacing Si−NH−Si linkages by $-O-SiCH_3$ groups.

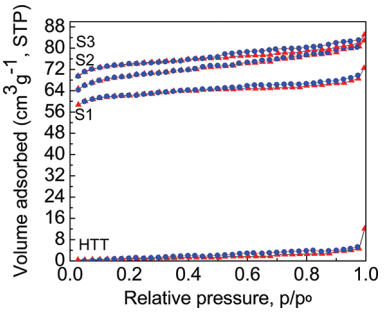

Figure 16. Nitrogen physisorption isotherms (red triangle, adsorption; blue circle, desorption) of the thermolysis products (i.e., Ni/Si−C−N−(O) nanocomposites) of the Ni−polysilazane precursors S1, S2, and S3 with the Ni(II) complex content of 6.3, 27, and 40 wt % used in the synthesis, respectively, manifesting the Type I isotherm, while the thermolysis product (i.e., Si−C−N−(O)) of the polysilazane HTT is nonporous.

Porosity Characteristics of Ni/Si−C−N−(O) Nanocomposites. Nitrogen physisorption isotherms manifest that the Si−C−N−(O) ceramics derived from the polysilazane HTT are nonporous, while the Ni/Si−C−N−(O) nanocomposites derived from the Ni−polysilazane precursors reveal type I isotherms which are typical for microporous materials (Figure 16) and possess specific surface area, micropore surface area, and micropore volume, e.g., 215, 205 $m^2\ g^{-1}$, and 0.113 $cm^3\ g^{-1}$, respectively, for the S3-derived Ni/Si−C−N−(O) nanocomposite. The specific surface area and the micropore volume of the Ni/Si−C−N−(O) nanocomposites increase with the nickel content (Figure 17b) as well as with the C/H and O/N ratios (Figure 17c, d). These features could be understood within the framework of the Gibbs nucleation theory,[67] addressing the nucleation and growth of the pores.

Generally, in polymer-derived ceramics, the nucleation of the pores is due to the volatization of decomposition products formed during the polymer-to-ceramic transformation. Further formation of volatile species at the nucleated pores walls leads to the pore growth. These processes induce a transient porosity in PDCs during the thermolysis; the latter is not stable, disappearing very fast as the thermolysis temperature increases.[29,68−71] For example, in the polysilazane-derived Si−C−N−(O) ceramics the pores starts to collapse at $T > 600$ °C,[29] i.e., Si−C−N−(O) ceramics pyrolyzed at 600 °C show type I isotherms with the specific surface area of about 350 $m^2\ g^{-1}$, whereas those

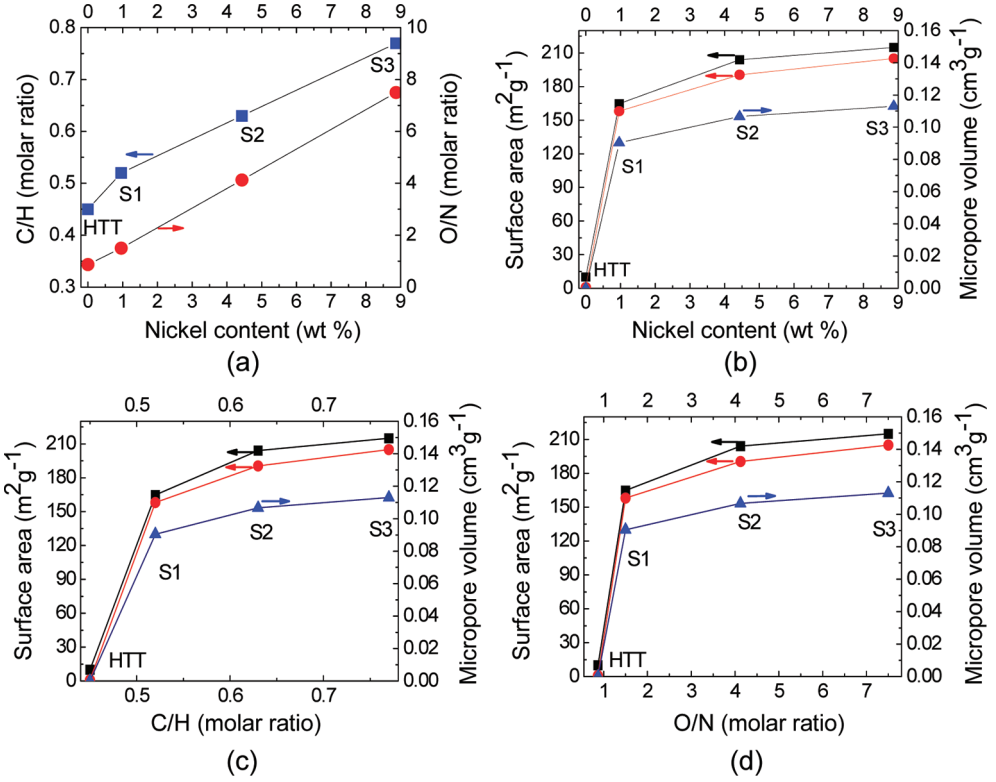

Figure 17. (a) C/H (carbon to hydrogen molar ratios) (blue square) and O/N (oxygen to nitrogen molar ratios) (red circle) in the Ni/Si−C−N−(O) nanocomposites as a function of nickel content, (b−d) specific surface area (black square), micropore surface area (red circle), and micropore volume (blue triangle) of the polysilazane HTT, and S1-, S2- and S3-derived ceramics, i.e., Si−C−N−(O) and Ni/Si−C−N−(O) nanocomposites, respectively, as a function of (b) nickel content, (c) C/H, and (d) O/N molar ratios.

dx.doi.org/10.1021/cm200589n |*Chem. Mater.* 2011, 23, 4112–4123

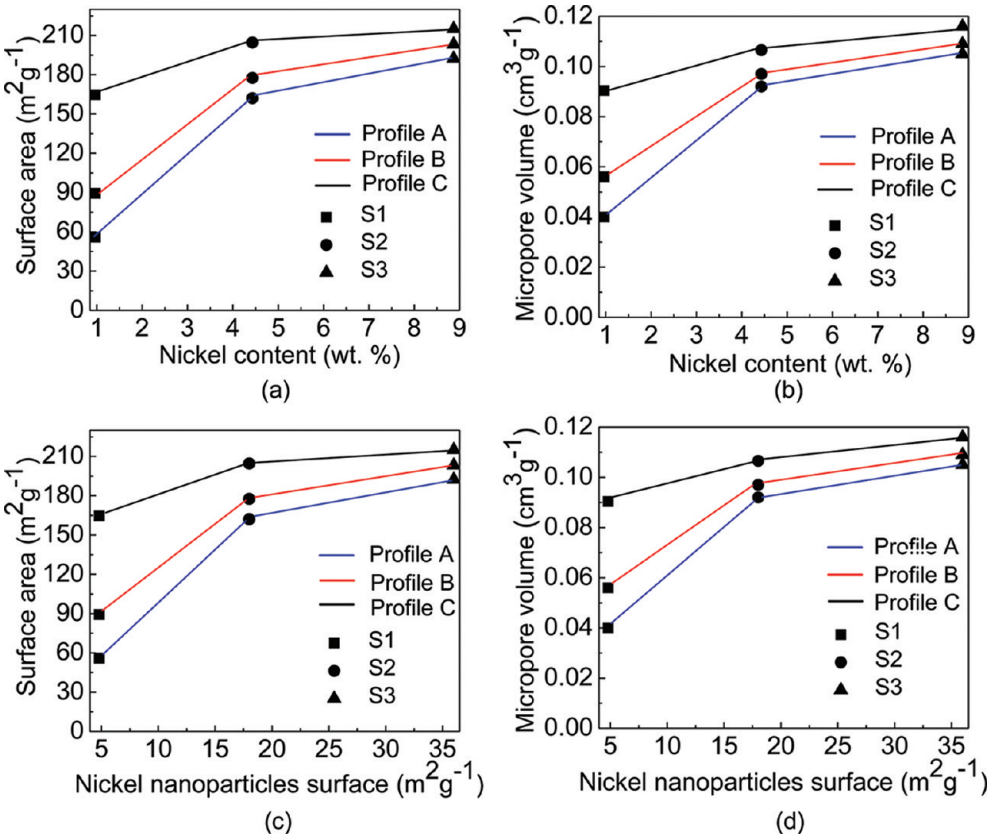

Figure 18. (a, c)Surface area and (b, d) micropore volume of the Ni/Si−C−N−(O) ceramics resulted from the Ni−polysilazane precursors S1, S2, and S3 with the Ni(II) complex content of 6.3, 27, and 40 wt % used in the synthesis, respectively, as a function of the measured nickel content (a, b) and the calculated specific surface area of nickel nanoparticles in the Ni/Si−C−N−(O) ceramics (c, d), thermolyzed according to the profile A, B, and C.

pyrolyzed at 700 °C have negligible porosity and specific surface area.[29]

The thermolysis profile C with the slow heating rate and the longest intermediate holding times (Figure 2) results in the formation of Ni/Si−C−N−(O) nanocomposites with the highest specific surface area and micropore volume (Figure 18; see also the Supporting Information, section Influence of the Thermolysis Profiles on the Porosity Development). Similar dependence of the specific surface area and the micropore volume on the thermolysis conditions have already been reported for microporous Si−C−N−(O) with SiC and AlN fillers.[29] The difference in the porosity characteristics can be attributed to the kinetics of reactions occurring during thermolysis, which is influenced by the heating rates and holding times.[29,68] Slow heating rates and long intermediate holding times (especially at early stages of the thermolysis) provide sufficient time for completing the cross-linking reactions, that stops the distillation of the polymer fragments during the later stages of the thermolysis which in turn reduces the abnormal pore growth. The specific surface area or the micropore volume of Ni/Si−C−N−(O) nanocomposites strongly depends on the nickel content of the Ni−polysilazane precursors (Figure 18) indicating the influence of the in situ formed nickel nanoparticles in the Ni−polysilazane precursors on the porosity development in Ni/Si−C−N−(O) nanocomposites most probably through the mechanism of heterogeneous nucleation of pores (refer to the section Influence of Nickel Content on the Porosity Development in the Supporting Information for additional discussions).[72] However, as the nickel nanoparticle content increases from sample S1 to S3, less difference was found in the specific surface area or the micropore volume of Ni/Si−C−N−(O) nanocomposites resulting from different thermolysis profiles (Figure 18). The similarity in the specific surface area and micropore volume of the Ni/Si−C−N−(O) nanocomposites with high in situ formed nickel nanoparticles content (Ni−polysilazane precursors S2 and S3) is discussed to be due to the similar size and distribution of nickel nanoparticles (Figure 14).

As the formation mechanism, structure, composition and the porosity characteristics of the Ni/Si−C−N−(O) nanocomposites differ significantly from those of the Si−C−N−(O) ceramics, this implies a common mechanism involved in the formation of nickel nanoparticles, precipitation of turbostratic carbon and the development of porosity. These common features are as follows:

(i) The nickel nanoparticles in the Ni−polysilazane precursors reduce the critical barrier for the formation of gaseous species during the polymer-to-ceramic transformation and facilitate the heterogeneous nucleation of pores due to the release of gas molecules such as H_2 and CH_4.[72] As the rigid carbosilane bonds formed in the Ni−polysilazane precursors are not affected at the temperatures of transamination and exchange reactions (200−500 °C),[3,34] the distillation of large polymer fragments does not occur. In this way the formation of macropores and the abnormal pore growth is significantly constrained. Furthermore, higher cross-linking due to the formation of carbosilane units enhances the evolved pore stability during the polymer (Ni−polysilazane

dx.doi.org/10.1021/cm200589n |*Chem. Mater.* 2011, 23, 4112–4123

precursors) to ceramic nanocomposite (Ni/Si−C−N−(O)) transformation.[73]

(ii) The dehydrogenation-active nickel nanoparticles decrease the starting temperature of the formation of turbostratic carbon by some hundred degrees. The previous studies showed that the turbostratic carbon reinforces the mechanical stability of the surrounding matrices.[74] This effect could be easily understood if we consider the structure of turbostratic carbon as being constructed of hexagonal basal planes of perfect graphene sheets which are randomly rotated along the *c* axis (instead of regular ... ABAB... stacking),[75] graphene itself possesses the highest intrinsic strength.[76] Accordingly, the turbostratic carbon with higher mechanical stability than that of the neighboring nanoporous matrix behaves as in situ formed nanofiller, and subsequently reinforces the nanoporous structure and reduces the nanopores collapse as a result of viscous flow,[68,69,71] stabilizing the micro/mesoporosity developed in the entire matrix of the Ni/Si−C−N−(O) nanocomposites.

CONCLUSIONS

In summary, a novel strategy to synthesize nanoporous ceramics is proposed. The addition of a Ni(II) complex to a polysilazane effectively turn a nonporous polymer derived ceramic to a nanoporous material. Nickel nanoparticles formed in situ during the synthesis of Ni−polysilazane precursors play a major role in modifying the mechanism of polymer-to-ceramic transformation. They facilitate the precipitation of turbostratic carbon and the heterogeneous nucleation of pores. Furthermore, replacement of unstable silazane linkages by stable carbosilane bonds which are not affected by the main polymer chain depolymerization during thermolysis, prohibits the distillation of small polymer fragments limiting pore growth and formation of macrovoids.

ASSOCIATED CONTENT

Supporting Information. Results of the ^{1}H, ^{13}C, ^{29}Si NMR, and STA−MS characterizations for the Ni−polysilazane precursors, FTIR of the Ni/Si−C−N−(O) nanocomposites. Further details of the reaction mechanisms involved in the synthesis of the Ni−polysilazane precursors. This material is available free of charge via the Internet at http://pubs.acs.org/.

AUTHOR INFORMATION

Corresponding Author

*E-mail: mseifba@materials.tu-darmstadt.de.

ACKNOWLEDGMENT

This work has been performed within the framework of the project "Thermoresistant ceramic membrane with integrated gas sensor for high temperature separation and detection of hydrogen and carbon monoxide" of the priority program "Adapting surfaces for high temperature applications" (DFG-SPP 1299, www.spp-haut.de, DFG-German Research Foundation). We thank Dr. Reinhard Meusinger for performing NMR measurements, Ravi Mohan Prasad for helping in BET measurements, and Dr. Emanuel Ionescu and Dr. Gabriela Mera for the fruitful discussions. R.R. thanks the Fonds der Chemischen Industrie, Frankfurt, Germany, for continuous financial support. A.G. acknowledges the Alexander-von-Humboldt Foundation for financial support.

REFERENCES

(1) Yeon, S. H.; Knoke, I.; Gogotsi, Y.; Fischer, J. E. *Microporous Mesoporous Mater.* **2010**, *131*, 423.
(2) Kockrick, E.; Schrage, C.; Borchardt, L.; Klein, N.; Rose, M.; Senkovska, I.; Kaskel, S. *Carbon* **2010**, *48*, 1707.
(3) Colombo, P.; Riedel, R.; Soraru, G. D.;Kleebe, H. J., *Polymer Derived Ceramics: From Nano-Structure to Applications*; DEStech Publications: Lancaster, PA, 2010; p 476.
(4) Briceno, K.; Garcia-Valls, R.; Montane, D. *Asia-Pacific J. Chem. Eng.* **2010**, *5*, 169.
(5) Schuth, F. *Eur. Phys. J.−Spec. Top.* **2009**, *176*, 155.
(6) Hassan, S.; Hector, A. L.; Hyde, J. R.; Kalaji, A.; Smith, D. C. *Chem. Commun.* **2008**, 5304.
(7) Colombo, P. *Science* **2008**, *322*, 381.
(8) Yang, C. M.; Lin, H. A.; Zibrowius, B.; Spliethoff, B.; Schueth, F.; Liou, S. C.; Chu, M. W.; Chen, C. H. *Chem. Mater.* **2007**, *19*, 3205.
(9) Ockwig, N. W.; Nenoff, T. M. *Chem. Rev.* **2007**, *107*, 4078.
(10) Lu, A. H.; Li, W. C.; Hou, Z. S.; Schuth, F. *Chem. Commun.* **2007**, 1038.
(11) Schuth, F. *Nature* **2005**, *434*, 712.
(12) Kamperman, M.; Garcia, C. B. W.; Du, P.; Ow, H. S.; Wiesner, U. *J. Am. Chem. Soc.* **2004**, *126*, 14708.
(13) Bradley, J. S.; Vollmer, O.; Rovai, R.; Specht, U.; Lefebvre, F. *Adv. Mater.* **1998**, *10*, 938.
(14) Iwamoto, Y.; Sato, K.; Kato, T.; Inada, T.; Kubo, Y. *J. Eur. Ceram. Soc.* **2005**, *25*, 257.
(15) Yoshida, K.; Ikuhara, Y. H.; Takahashi, S.; Hirayama, T.; Saito, T.; Sueda, S.; Tanaka, N.;Gai, P. L. *Nanotechnology* **2009**, *20*.
(16) Gu, Y. F.; Oyama, S. T. *J. Membr. Sci.* **2009**, *345*, 267.
(17) Boffa, V.; Castricum, H. L.; Garcia, R.; Schmuhl, R.; Petukhov, A. V.; Blank, D. H. A.; ten Elshof, J. E. *Chem. Mater.* **2009**, *21*, 1822.
(18) Igi, R.; Yoshioka, T.; Ikuhara, Y. H.; Iwamoto, Y.; Tsuru, T. *J. Am. Ceram. Soc.* **2008**, *91*, 2975.
(19) Boffa, V.; ten Elshof, J. E.; Petukhov, A. V.; Blank, D. H. A. *ChemSusChem* **2008**, *1*, 437.
(20) Ikuhara, Y. H.; Mori, H.; Saito, T.; Iwamoto, Y. *J. Am. Ceram. Soc.* **2007**, *90*, 546.
(21) Yamazaki, S.; Uno, N.; Mori, H.; Ikuhara, Y. H.; Iwamoto, Y.; Kato, T.; Hirayama, T. *J. Mater. Sci.* **2006**, *41*, 2679.
(22) de Vos, R. M.; Verweij, H. *Science* **1998**, *279*, 1710.
(23) Oyama, S. T.; Lee, D.; Hacarlioglu, P.; Saraf, R. F. *J. Membr. Sci.* **2004**, *244*, 45.
(24) Prasad, R. M.; Iwamoto, Y.; Riedel, R.; Gurlo, A. *Adv. Eng. Mater.* **2010**, *12*, 522.
(25) Colombo, P.; Mera, G.; Riedel, R.; Soraru, G. D. *J. Am. Ceram. Soc.* **2010**, *93*, 1805.
(26) Riedel, R.; Kleebe, H. J.; Schonfelder, H.; Aldinger, F. *Nature* **1995**, *374*, 526.
(27) Manocha, L. M.; Manocha, S. M. *Carbon* **1995**, *33*, 435.
(28) Prasad, R. M.; Gurlo, A.; Riedel, R.; Hubner, M.; Barsan, N.; Weimar, U. *Sens. Actuators, B* **2010**, *149*, 105.
(29) Dismukes, J. P.; Johnson, J. W.; Bradley, J. S.; Millar, J. M. *Chem. Mater.* **1997**, *9*, 699.
(30) Nagata, K.; Miyamoto, M.; Fujioka, Y.; Yogo, K. *Desalin. Water Treat.* **2010**, *17*, 233.
(31) Chavez, R.; Ionescu, E.; Balan, C.; Fasel, C.; Riedel, R. *J. Appl. Polym. Sci.* **2011**, *119*, 794.
(32) Li, Y. L.; Kroke, E.; Riedel, R.; Fasel, C.; Gervais, C.; Babonneau, F. *Appl. Organomet. Chem.* **2001**, *15*, 820.
(33) Markelov, D. A.; Matveev, V. V.; Ingman, P.; Nikolaeva, M. N.; Lahderanta, E.; Shevelev, V. A.; Boiko, N. I. *J. Phys. Chem. B* **2010**, *114*, 4159.

(34) Yive, N. S. C. K.; Corriu, R. J. P.; Leclercq, D.; Mutin, P. H.; Vioux, A. *Chem. Mater.* **1992**, *4*, 141.
(35) Jones, G. D.; Martin, J. L.; McFarland, C.; Allen, O. R.; Hall, R. E.; Haley, A. D.; Brandon, R. J.; Konovalova, T.; Desrochers, P. J.; Pulay, P.; Vicic, D. A. *J. Am. Chem. Soc.* **2006**, *128*, 13175.
(36) Jones, G. D.; McFarland, C.; Anderson, T. J.; Vicic, D. A. *Chem Commun* **2005**, 4211.
(37) Gibson, V. C.; Spitzmesser, S. K. *Chem. Rev.* **2003**, *103*, 283.
(38) Britovsek, G. J. P.; Gibson, V. C.; Wass, D. F. *Angew. Chem., Int. Ed.* **1999**, *38*, 428.
(39) Kiso, Y.; Kumada, M.; Tamao, K.; Umeno, M. *J. Organomet. Chem.* **1973**, *50*, 297.
(40) Kiso, Y.; Kumada, M.; Maeda, K.; Sumitani, K.; Tamao, K. *J. Organomet. Chem.* **1973**, *50*, 311.
(41) Briendfaure, M.; Jeanjean, J.; Kermarec, M.; Delafosse, D. *J Chem Soc Farad T 1* **1978**, *74*, 1538.
(42) Wang, Z. X.; Huang, F.; Zhang, C. G.; Jiang, J. L.; Guan, H. R. *Inorg. Chem.* **2011**, *50*, 3816.
(43) Prakash, G. K. S.; Do, C.; Mathew, T.; Olah, G. A. *Catal. Lett.* **2011**, *141*, 507.
(44) Yulikov, M. M.; Purtov, P. A. *Appl. Magn. Reson.* **2005**, *29*, 231.
(45) Francis, A.; Ionescu, E.; Fasel, C.; Riedel, R. *Inorg. Chem.* **2009**, *48*, 10078.
(46) Scheffler, M.; Greil, P.; Berger, A.; Pippel, E.; Woltersdorf, J. *Mater. Chem. Phys.* **2004**, *84*, 131.
(47) Bengaard, H. S.; Norskov, J. K.; Sehested, J.; Clausen, B. S.; Nielsen, L. P.; Molenbroek, A. M.; Rostrup-Nielsen, J. R. *J. Catal.* **2002**, *209*, 365.
(48) Leclercq, G.; Pietrzyk, S.; Peyrovi, M.; Karroua, M. *J. Catal.* **1986**, *99*, 1.
(49) Bally, T.; Masamune, S. *Tetrahedron* **1980**, *36*, 343.
(50) Cram, D. J. *Nature* **1992**, *356*, 29.
(51) Cram, D. J.; Tanner, M. E.; Thomas, R. *Angew Chem Int Edit* **1991**, *30*, 1024.
(52) Maier, G. *Angew. Chem., Int Ed.* **1974**, *13*, 425.
(53) Maier, G. *Angew. Chem., Int Ed.* **1988**, *27*, 309.
(54) Watts, L.; Fitzpatr., Jd; Pettit, R. *J. Am. Chem. Soc.* **1965**, *87*, 3253.
(55) Watts, L.; Pettit, R. *Adv. Chem. Ser.* **1967**, 549.
(56) El-Shall, M. S.; Momoh, P. O.; Abrash, S. A.; Mabrouki, R. *J. Am. Chem. Soc.* **2006**, *128*, 12408.
(57) Epstein, E. F.; Dahl, L. F. *J. Am. Chem. Soc.* **1970**, *92*, 502.
(58) Mauret, P.; Guerch, G.; Martin, S. *C. R. Acad. Sci., Ser. IIc: Chim.* **1977**, *284*, 747.
(59) Pitzer, R. M.; Goddard, J. D.; Schaefer, H. F. *J. Am. Chem. Soc.* **1981**, *103*, 5681.
(60) Sicilia, E.; Russo, N. *J. Mol. Struct.—Theochem* **2004**, *709*, 167.
(61) Coll, R.; Salvado, J.; Farriol, X.; Montane, D. *Fuel Process. Technol.* **2001**, *74*, 19.
(62) Li, Y.; Houk, K. N. *J. Am. Chem. Soc.* **1996**, *118*, 880.
(63) Mera, G.; Riedel, R.; Poli, F.; Muller, K. *J. Eur. Ceram. Soc.* **2009**, *29*, 2873.
(64) Turquat, C.; Kleebe, H. J.; Gregori, G.; Walter, S.; Soraru, G. D. *J. Am. Ceram. Soc.* **2001**, *84*, 2189.
(65) Ziegler, G.; Kleebe, H. J.; Motz, G.; Muller, H.; Trassl, S.; Weibelzahl, W. *Mater. Chem. Phys.* **1999**, *61*, 55.
(66) Kleebe, H. J. *Phys. Status Solidi A* **1998**, *166*, 297.
(67) Kashchiev, D., *Nucleation: Basic Theory with Applications*; Butterworth Heinemann: Oxford, U.K., 2000.
(68) Sanchez-Jimenez, P. E.; Downs, J. A.; Raj, R. *J. Am. Ceram. Soc.* **2010**, *93*, 2567.
(69) Lipowitz, J.; Rabe, J. A.; Frevel, L. K.; Miller, R. L. *J. Mater. Sci.* **1990**, *25*, 2118.
(70) Galusek, D.; Reschke, S.; Riedel, R.; Dressler, W.; Sajgalik, P.; Lencees, Z.; Majling, J. *J. Eur. Ceram. Soc.* **1999**, *19*, 1911.
(71) Borek, T. T.; Ackerman, W.; Hua, D. W.; Paine, R. T.; Smith, D. M. *Langmuir* **1991**, *7*, 2844.
(72) Izaak, T. I.; Babkina, O. V.; Lyamina, G. V.; Svetlichnyi, V. A. *Russian J. Phys. Chem. A* **2008**, *82*, 2111.
(73) Williams, H. M.; Dawson, E. A.; Barnes, P. A.; Rand, B.; Brydson, R. M. D.; Brough, A. R. *J. Mater. Chem.* **2002**, *12*, 3754.
(74) Chasiotis, I.; Ozkan, T.; Naraghi, M. *Carbon* **2010**, *48*, 239.
(75) Sjostrom, H.; Ivanov, I.; Johansson, M.; Hultman, L.; Sundgren, J. E.; Hainsworth, S. V.; Page, T. F.; Wallenberg, L. R. *Thin Solid Films* **1994**, *246*, 103.
(76) Hone, J.; Lee, C.; Wei, X. D.; Kysar, J. W. *Science* **2008**, *321*, 385.